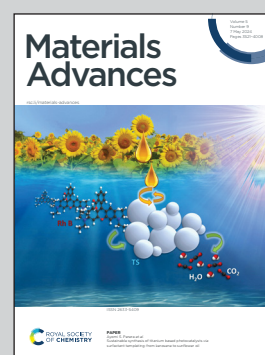


Showcasing research from Professor Ignas Kenfack Tonlé's laboratory, Electrochemistry and Chemistry of Materials, Research Unit of Noxious Chemistry and Environmental Engineering, Department of Chemistry, University of Dschang, West Region, Cameroon.

Evaluation of two core-shell ( $\text{Ag}_2\text{S}@-$  and  $\text{Bi}_2\text{S}_3@-$ ) sensors based on a metal-organic framework ( $\text{NH}_2\text{-MIL-125-Ti}$ )/ polyaniline for the electroanalysis of uric acid in urine samples

This work reports the potential of titanium-based metal organic framework (MOF,  $\text{NH}_2\text{-MIL-125(Ti)}$ ) as sensing materials based on its properties, such as high surface area, high porosity, good stability, and good electrocatalytic ability. This MOF has been improved through coating with core-shells of silver (Ag) and Bismuth (Bi) in the presence of a conducting polymer (polyaniline, PANI) to form two composites on the glassy carbon surface  $\text{Ag}_2\text{S}@ \text{NH}_2\text{-MIL-125(Ti)}/\text{PANI}/\text{GCE}$  and  $\text{Bi}_2\text{S}_3@ \text{NH}_2\text{-MIL-125(Ti)}/\text{PANI}/\text{GCE}$ , which were used for the electrochemical detection of uric acid.

### As featured in:



See Gullit Deffo,  
Cyrille Ghislain Fotsop *et al.*,  
*Mater. Adv.*, 2024, 5, 3683.

Cite this: *Mater. Adv.*, 2024,  
5, 3683

## Evaluation of two core–shell ( $\text{Ag}_2\text{S}@$ - and $\text{Bi}_2\text{S}_3@$ -) sensors based on a metal–organic framework ( $\text{NH}_2$ -MIL-125-Ti)/polyaniline for the electroanalysis of uric acid in urine samples†

Gullit Deffo,<sup>id</sup>\*<sup>ab</sup> Cyrille Ghislain Fotsop,<sup>\*ac</sup> Marcel Cédric Deussi Ngaha,<sup>ad</sup> Sengor Gabou Fogang,<sup>a</sup> Lionnel Averie Vomo,<sup>a</sup> Bibiane Wandji Nkuigoua,<sup>a</sup> Calmette Akenmo Shella,<sup>a</sup> Alex Vincent Somba,<sup>a</sup> Thierry Flavien Nde Tene,<sup>a</sup> Ida Kouam Tchummegne,<sup>ae</sup> Evangeline Njanja,<sup>a</sup> Ignas Kenfack Tonlé,<sup>id</sup><sup>a</sup> Panchanan Puzari<sup>id</sup><sup>b</sup> and Emmanuel Ngamenif

Chemical sensors for the determination of uric acid (UA) in human urine samples have been developed using a composite material based on two core–shells ( $\text{Ag}_2\text{S}@$ - and  $\text{Bi}_2\text{S}_3@$ -) coated with a metal–organic framework ( $\text{NH}_2$ -MIL-125-Ti) and polyaniline (PANI). The composite materials were characterized using Fourier transform infra-red (FTIR) spectroscopy, X-ray diffraction (XRD), scanning electron microscopy (SEM), energy dispersive X-ray (EDX/EDX-mapping),  $\text{N}_2$  adsorption–desorption, thermal gravimetric analysis/differential thermogravimetry (TGA/DTG), cyclic voltammetry (CV), and electrochemical impedance spectroscopy (EIS) techniques. Differential pulse voltammetry (DPV) studies show that the oxidation peak current of UA obtained with  $\text{Ag}_2\text{S}@$  $\text{NH}_2$ -MIL-125(Ti)/PANI/GCE and  $\text{Bi}_2\text{S}_3@$  $\text{NH}_2$ -MIL-125(Ti)/PANI/GCE is respectively 2.45 and 2.31 times higher than the one obtained with a bare glassy carbon electrode (GCE). Calibration curves from 0 to 16  $\mu\text{M}$  UA were generated after the optimization of critical parameters affecting the detection limit of UA. The sensitivities and limits of detection (LOD) obtained were 299.0  $\mu\text{A mM}^{-1}$  and 0.579  $\mu\text{M}$ , 263.0  $\mu\text{A mM}^{-1}$  and 0.446  $\mu\text{M}$  for  $\text{Ag}_2\text{S}@$  $\text{NH}_2$ -MIL-125(Ti)/PANI/GCE and  $\text{Bi}_2\text{S}_3@$  $\text{NH}_2$ -MIL125(Ti)/PANI/GCE, respectively. The developed sensors show good selectivity, reproducibility, repeatability and storage stability at room temperature. Finally, the sensor was successfully applied for the determination of UA in human urine samples. The sensors were able to detect UA in human urine samples even after 200 times dilution, offering new hope for future point-of-care testing (POCT) devices for uric acid analysis.

Received 28th December 2023,  
Accepted 13th February 2024

DOI: 10.1039/d3ma01182h

rsc.li/materials-advances

## 1. Introduction

In recent time, research on the development of electrochemical sensors and biosensors for human pathological samples has been drawing significant attention owing to their advantages such

as improved sensitivity, operational simplicity, cost efficiency and the scope of converting to wearable miniaturized devices suitable for point-of-care testing (POCT) applications.<sup>1–3</sup> The conventional analytical methods for these pathological samples include spectroscopic,<sup>4,5</sup> chromatographic,<sup>6,7</sup> enzyme-colorimetric<sup>8</sup> and capillary electrophoresis.<sup>9</sup> These methods require costly analytical instruments, trained personnel for analysis and they are time consuming which make them unsuitable for POCT application. In this regard, electrochemical methods are used as an alternative and promising strategy to achieve the objective of elaboration of point-of-care devices, especially for application in medicine. Medicinal compounds with more interest are found in the pathological samples. Uric acid (UA) is one of the compounds most frequently found in pathological samples. The amount of this species is the marker of health conditions of a human being as its low level as well as high level can cause different adverse health effects. In the human body, UA is produced by the metabolism of cells and purines.<sup>10</sup> It provides an antioxidant defence in humans

<sup>a</sup> Electrochemistry and Chemistry of Materials, Department of Chemistry, Faculty of Science, University of Dschang, P. O. Box 67, Dschang, Cameroon.

E-mail: gullitdeffo@gmail.com, fotsopcyril@yahoo.fr

<sup>b</sup> Department of Chemical Sciences, Tezpur University, Tezpur, Assam 784028, India

<sup>c</sup> Institute of Chemistry, Faculty of Process and Systems Engineering, Universitätsplatz 2, 39106 Magdeburg, Germany

<sup>d</sup> Department of Chemistry, Higher Teacher Training College, University of Bamenda, Bamili P. O. Box. 39, Cameroon

<sup>e</sup> Center for the Environment, Indian Institute of Technology Guwahati, Guwahati 781039, Assam, India

<sup>f</sup> University of Yaoundé 1, Faculty of Science, Department of Chemistry, Laboratory of Analytical Chemistry, P. O. Box 812, Yaoundé, Cameroon

† Electronic supplementary information (ESI) available. See DOI: <https://doi.org/10.1039/d3ma01182h>

against oxidants and radicals, thereby, helping in the prevention of aging and cancer.<sup>11</sup> Elevated levels of UA can cause hyperuricemia and gout and are closely related to other pathological symptoms such as fatty liver,<sup>11</sup> heart disease,<sup>12</sup> Parkinson's disease,<sup>13</sup> atherosclerosis,<sup>14</sup> kidney disease<sup>15</sup> and Lesch-Nyhan syndrome.<sup>16</sup> On the other hand, a low level of uric acid can cause certain genetic diseases.<sup>17,18</sup> Due to the biomedical significance of UA, currently, the development of electrochemical sensors for its fast and low-cost effective quantification in physiological samples is gaining much research attention. Electrochemical methods for its determination in physiological samples face the problem that the oxidation potential of UA is close to some of the other compounds such as ascorbic acid, dopamine, acetaminophen, *etc.*, thus interfering the analysis of one species by the other.<sup>19</sup> Moreover, in physiological samples, uric acid is present at concentrations ranging from 160 to 500  $\mu\text{M}$ .<sup>20–22</sup> Therefore, the challenge while developing electrochemical sensors for this species is to prepare a receptor selective for the target analyte and which can detect it at a concentration in the physiological range or even less than that. Electrochemical sensors based on modification of a glassy carbon electrode (GCE) with different graphene-based composite materials show promising results in overcoming this problem. Such modifications include modification with PVP-graphene composites,<sup>23</sup> reduced graphene oxide-palladium nanocomposites,<sup>24</sup> titanium nitride-reduced graphene oxide composites,<sup>25</sup> poly(sodium-4-styrenesulphonate) functionalized 3D graphene,<sup>26</sup> holey nitrogen-doped graphene aerogels,<sup>27</sup> and Ag nanoparticle-graphene oxide-poly(L-arginine) composites.<sup>28</sup> Due to the increasing environmental awareness, in recent years, a significant research focus has been directed towards the utilization of biomass materials for the development of practical and value-added products including chemical sensors.<sup>29</sup> Recently, Qi *et al.* have prepared Au nanoparticle-loaded egg shell  $\text{CaCO}_3$  composites for developing a nitrite sensor.<sup>30</sup> Some research groups have reported the development of enzyme immobilization-based biosensors using an egg shell membrane (ESM) as the immobilization matrix.<sup>31</sup> In our previous works, we have developed UA sensors and biosensors, based on biomass materials such as egg shell nano- $\text{CaCO}_3$  and palm oil fibers.<sup>22–32</sup> The design of new sensing materials for the detection of this physiological compound with higher sensitivity and resolution remains an area requiring much more work as the strategies for the development of wearable sensors are the final goal.<sup>33</sup> Metal-organic frameworks (MOFs) as a new class of electrode materials offering new hope in this regard due to the synergistic catalytic behaviour and the electroactivity of the incorporated metals in MOFs.<sup>34</sup> Nowadays, the utilization of MOFs as catalysts has attracted more and more attention owing to their versatile structures, topologies and composition, tunable functionalities, and highly ordered porous structure.<sup>35</sup> They are crystalline materials made of organic linkers coordinatively connecting to metal-oxo clusters to yield a void-containing network.<sup>36</sup> MOFs are known to have characteristics such as high porosity, high hydrothermal and chemical stability, and a large Brunauer-Emmett-Teller (BET)-specific surface area.<sup>36</sup> Despite many promising advantages, the applications of MOFs in catalytic

reactions are still largely restricted, mainly in terms of low activity caused by the blockage of active metal centers by organic linkers and the instability for recycling.<sup>37</sup> To overcome the limitations, different kinds of strategies have been proposed including either introducing additional components into MOFs or pyrolyzing MOFs into different functional materials.<sup>35,38,40</sup> Particularly, the latter route is much attractive due to the advantages of MOFs as precursors, such as flexible designability on compositions and micro/nanostructures, templating effect, and low cost.  $\text{NH}_2\text{-MIL-125}(\text{Ti})$ , a porous amino-functionalized titanium based MOF, has been proved to be an efficient and stable support for metallic nanoparticles (Pd, Pt, and Au) and the resulting composites exhibited excellent heterogeneous catalytic performance.<sup>41</sup> Improving the catalytic capacity of MOFs by coating their surface with metal particles to form core-shells has recently received high interest as a new avenue of research.<sup>35–41</sup> Additionally, polymer materials reputed to be good conductors such as polyaniline would contribute to the signal amplification of an analyte. Polyaniline (PANI) is one of the most significant conducting polymers due to its facile preparation, tunable conductivity and high environmental stability. Thus, considerable efforts have been devoted to improving its unique electronic, optical and electrochemical properties, as well as the extensive applications in optical sensing and bio-electrochemical sensing.<sup>42</sup> Taken together, the  $\text{NH}_2\text{-MIL-125}(\text{Ti})$  coated core-shell with PANI, to the best of our knowledge, has never been explored. In this work, composites of polyaniline and two core-shells@MOFs have been used to modify a bare GCE by drop coating and drying to form sensors labelled as  $\text{Ag}_2\text{S@NH}_2\text{-MIL-125}(\text{Ti})/\text{PANI}/\text{GCE}$  and  $\text{Bi}_2\text{S}_3\text{@NH}_2\text{-MIL-125}(\text{Ti})/\text{PANI}/\text{GCE}$ , used for the sensing of UA in urine samples. This work has not only demonstrated a novel use of core-shell-coated MOFs and polymer materials for a useful purpose, but it also shades new hopes for a potential alternative to the dependence on derived carbon materials in this field.

## 2. Materials and methods

### 2.1. Materials

All chemicals and reagents were used as received without any purification. They included HCl (35%) and ammonium peroxydisulfate ( $(\text{NH}_4)_2\text{S}_2\text{O}_8$  (98%) from Emplura; gelatin from porcine skin;  $\text{K}_3\text{Fe}(\text{CN})_6$  (99%) and NaOH (98%) from Rankem;  $\text{K}_2\text{HPO}_4$  (99%),  $\text{KH}_2\text{PO}_4$  (99%), and KCl (99.5%) from Merck; 2-amino terephthalic acid (99%), titanium isopropoxide (99.8%), *N,N*-dimethylformamide (DMF, 99.8%), anhydrous methanol (99.8%), bismuth nitrate  $\text{Bi}(\text{NO}_3)_3 \cdot 5\text{H}_2\text{O}$  (99.5%), silver nitrate  $\text{AgNO}_3$  (99.8%), thiourea (98%), and uric acid (99%) were purchased from Sigma-Aldrich. Aniline, acetone and all other chemicals were purchased from Merck, Fisher and SRL.

### 2.2. Synthesis of materials and preparation of working electrodes

$\text{NH}_2\text{-MIL-125}(\text{Ti})$  was synthesized using the solvothermal method as previously described<sup>43,44</sup> with modifications, briefly described in the ESI† (SI-1). The synthesis of  $\text{Ag}_2\text{S@NH}_2\text{-MIL-125}(\text{Ti})$





125(Ti) and  $\text{Bi}_2\text{S}_3@\text{NH}_2\text{-MIL-125(Ti)}$  is adapted from the method proposed<sup>45,46</sup> with slight modifications shown in SI-2 (ESI†). Polyaniline (PANI) was synthesized using the method described (SI-3, ESI†).<sup>32–47</sup> The geometric surface of the bare glassy carbon electrode (GCE) used ( $0.071\text{ cm}^2$ ) was calculated using the formula  $S = \pi r^2$ , where  $\pi = 3.14$  and the geometric radius  $r = 0.15\text{ cm}$ . Prior to its modification, the bare GCE was polished with alumina powder ( $0.3\text{ }\mu\text{m}$  size) and then sonicated in 1:1 ethanol–water solution for 5 min. 4 mg of  $\text{Ag}_2\text{S}@\text{NH}_2\text{-MIL-125(Ti)}$  or  $\text{Bi}_2\text{S}_3@\text{NH}_2\text{-MIL-125(Ti)}$  and 2 mg of PANI were dispersed in 1 mL (1:1) of DMF/gelatin (5%) by ultrasonication for 30 min to give a homogeneous dispersion of  $\text{Ag}_2\text{S}@\text{NH}_2\text{-MIL-125(Ti)}/\text{PANI}$  or  $\text{Bi}_2\text{S}_3@\text{NH}_2\text{-MIL-125(Ti)}/\text{PANI}$ . The clean GCE surface was then coated with 5  $\mu\text{L}$  of resulting dispersions and dried in an oven at  $40\text{ }^\circ\text{C}$  for 15 min to obtain a thin film on the working electrode (referred as  $\text{Ag}_2\text{S}@\text{NH}_2\text{-MIL-125(Ti)}/\text{PANI}/\text{GCE}$  and  $\text{Bi}_2\text{S}_3@\text{NH}_2\text{-MIL-125(Ti)}/\text{PANI}/\text{GCE}$ ). For comparison studies, bare GCE,  $\text{Ag}_2\text{S}/\text{GCE}$ ,  $\text{Bi}_2\text{S}_3/\text{GCE}$ ,  $\text{NH}_2\text{-MIL-125(Ti)}/\text{GCE}$ ,  $\text{PANI}/\text{GCE}$ ,  $\text{Ag}_2\text{S}@\text{NH}_2\text{-MIL-125(Ti)}/\text{GCE}$  and  $\text{Bi}_2\text{S}_3@\text{NH}_2\text{-MIL-125(Ti)}/\text{GCE}$  were also prepared using similar procedures.

### 2.3. Physicochemical and electrochemical procedures

The physicochemical characterizations of  $\text{NH}_2\text{-MIL-125(Ti)}$ ,  $\text{Ag}_2\text{S}$ ,  $\text{Bi}_2\text{S}_3$ ,  $\text{Ag}_2\text{S}@\text{NH}_2\text{-MIL-125(Ti)}$ ,  $\text{Bi}_2\text{S}_3@\text{NH}_2\text{-MIL-125(Ti)}$ ,  $\text{PANI}$ ,  $\text{Ag}_2\text{S}@\text{NH}_2\text{-MIL-125(Ti)}/\text{PANI}$ , and  $\text{Bi}_2\text{S}_3@\text{NH}_2\text{-MIL-125(Ti)}/\text{PANI}$  were performed *via* (i) Fourier transform infrared (FTIR) spectroscopy conducted in the range of  $4000\text{--}200\text{ cm}^{-1}$  using a spectrometer, specifically the “Nicolet iS50” model from Thermo Scientific, (ii) X-ray diffraction (XRD) recorded using  $\text{CuK}\alpha$  radiation with wavelength ( $\lambda = 1.5406\text{ \AA}$ ) on an MPD X’Pert Pro diffractometer (PANalytical), equipped with an X’Celerator detector, (iii) scanning electron microscopy/energy dispersive X-ray (SEM/EDX/SEM-mapping) using SEM (XL30 FESEM from FEI, Hillsboro) equipped with an EDX Genesis Energy Dispersive X-ray Detector, (iv) Brunauer–Emmett–Teller (BET) analysis using  $\text{N}_2$  adsorption–desorption isotherms, measured with a 3Flex share instrument from Micrometrics GmbH, Norcross, and (v) thermal gravimetric analysis/differential thermogravimetry (TGA/DTG) analyses using an STA 449C Jupiter instrument from Netzsch, Selb, Germany. Cyclic voltammetry (CV) and electrochemical impedance spectroscopic (EIS) techniques were used for the characterization of modified electrodes, while a differential pulse voltammetry (DPV) technique was used for the quantitative measurement of the uric acid (UA) analyte, and chronoamperometry (CA) was used for the interference studies. The conventional system of three electrodes was used, with the bare and modified GCE as a working electrode, platinum wire as an auxiliary electrode and  $\text{Ag}/\text{AgCl}$  (3 M KCl) as a reference electrode. Cyclic voltammograms were recorded from  $-0.80$  to  $1.0\text{ V}$  and from  $-0.050$  to  $0.850\text{ V}$  at a scan rate of  $50\text{ mV s}^{-1}$ , respectively, in 3 mL of 5 mM  $[\text{Fe}(\text{CN})_6]^{3-/4-}$  (0.1 M KCl, pH 7.0) and 1 mM UA (PB, pH 7.0). Differential pulse voltammograms were recorded from  $-0.20\text{ V}$  to  $0.90\text{ V}$  at step potential:  $5\text{ mV}$ ; amplitude:  $60\text{ mV}$ ; pulse width:  $0.05\text{ s}$ ; sample width:  $0.01\text{ s}$  and

pulse period:  $0.2\text{ s}$  for all measurements, in 3 mL of UA solution in 0.1 M phosphate buffer (PB, pH 7.0). EIS was recorded in the frequency range from  $1.0\text{ kHz}$  to  $100.0\text{ kHz}$  at a potential of  $0.40\text{ V}$  using 5 mM  $[\text{Fe}(\text{CN})_6]^{3-/4-}$  in 0.10 M KCl. CA was conducted under pretreatment settings ( $E_{\text{condition}} = 0.450\text{ V}$ ,  $t_{\text{condition}} = 0.0\text{ s}$ ,  $E_{\text{deposition}} = 0.450\text{ V}$  and  $t_{\text{deposition}} = 5.0\text{ s}$ ), and under amperometric detection settings [ $t_{\text{equilibration}} = 5.0\text{ s}$ ,  $t_{\text{interval}} = 1.0\text{ s}$ ,  $t_{\text{run}} = 1000.0\text{ s}$ , and  $E_{\text{dc}} = 0.370\text{ V}$  ( $\text{Ag}_2\text{S}@\text{NH}_2\text{-MIL-125(Ti)}/\text{PANI}/\text{GCE}$ ) or  $0.440\text{ V}$  ( $\text{Bi}_2\text{S}_3@\text{NH}_2\text{-MIL-125(Ti)}/\text{PANI}/\text{GCE}$ )] in 50  $\mu\text{M}$  uric acid (0.10 M PB, pH 7.0) in the presence of 50  $\mu\text{M}$  of interfering agents. The electroanalytical experiments were carried out on a PalmSens 3 potentiostat controlled by a computer, equipped with PStace (version 4.8) software for recording electrochemical experimental curves, and Origin™ 6.0 and 18 softwares for plotting the curves. Measurements of pH were carried out with a Metrohm 780 pH meter equipped with a glass electrode.

## 3. Results and discussion

### 3.1. Physico-chemical characterization

**3.1.1. FTIR spectra.** The FTIR spectra of  $\text{NH}_2\text{-MIL-125(Ti)}$ ,  $\text{Ag}_2\text{S}$ ,  $\text{Bi}_2\text{S}_3$ ,  $\text{Ag}_2\text{S}@\text{NH}_2\text{-MIL-125(Ti)}$ ,  $\text{Bi}_2\text{S}_3@\text{NH}_2\text{-MIL-125(Ti)}$ ,  $\text{PANI}$ ,  $\text{Ag}_2\text{S}@\text{NH}_2\text{-MIL-125(Ti)}/\text{PANI}$ , and  $\text{Bi}_2\text{S}_3@\text{NH}_2\text{-MIL-125(Ti)}/\text{PANI}$  were recorded and are shown in Fig. 1. It appears on the spectrum of the MOF (a) that around  $3335\text{ cm}^{-1}$  a stretching vibration is assigned to the  $\text{NH}_2$  of the organic linker and the OH of the residual water and methanol.<sup>44</sup> At  $1536\text{ cm}^{-1}$  and  $1383\text{ cm}^{-1}$ , the vibration bands observed are characteristic of carboxylate linkers, and at  $1253\text{ cm}^{-1}$ , the peak observed can be attributed to the C–N and C–C stretching of the aromatic amine group.<sup>44,48,49</sup> The vibration around  $513\text{ cm}^{-1}$  corresponds to the Ti–O bond which occurred in the presence of the residual solvent methanol and water. In the spectra of  $\text{Ag}_2\text{S}$  (b) and  $\text{Bi}_2\text{S}_3$  (c), it is observed that they exhibit a similar pattern with their characteristic peaks between  $1047\text{ cm}^{-1}$  and  $153\text{ cm}^{-1}$ . Vibrations observed at  $2321\text{ cm}^{-1}$  and  $2079\text{ cm}^{-1}$  are assigned to the stretching and bending

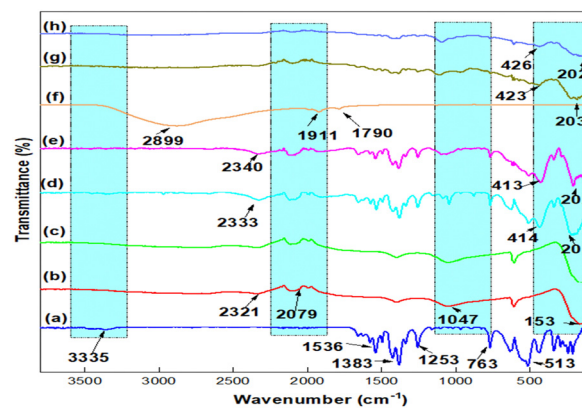


Fig. 1 FTIR spectra of (a)  $\text{NH}_2\text{-MIL-125(Ti)}$ , (b)  $\text{Ag}_2\text{S}$ , (c)  $\text{Bi}_2\text{S}_3$ , (d)  $\text{Ag}_2\text{S}@\text{NH}_2\text{-MIL-125(Ti)}$ , (e)  $\text{Bi}_2\text{S}_3@\text{NH}_2\text{-MIL-125(Ti)}$ , (f)  $\text{PANI}$ , (g)  $\text{Ag}_2\text{S}@\text{NH}_2\text{-MIL-125(Ti)}/\text{PANI}$ , and (h)  $\text{Bi}_2\text{S}_3@\text{NH}_2\text{-MIL-125(Ti)}/\text{PANI}$ .



vibrations of the  $\text{-OH}$  bond of the adsorbed water molecules.<sup>50,51</sup> Upon coating  $\text{Ag}_2\text{S}$  (b) and  $\text{Bi}_2\text{S}_3$  (c) on the surface of  $\text{NH}_2\text{-MIL-125(Ti)}$  to form the core-shells  $\text{Ag}_2\text{S@NH}_2\text{-MIL-125(Ti)}$  and  $\text{Bi}_2\text{S}_3\text{@NH}_2\text{-MIL-125(Ti)}$  shown by the spectra (d) and (e), respectively, it is observed that peaks assigned previously to the MOF (a), to the sulphide metals (b), and to the bismuth metals (c) are all present in the pattern of (d) and (e). This means that core-shell assembling is a method which does not destroy the functional groups present in the single materials. Fig. 1(f) shows the spectra of PANI where a large band between  $3500\text{ cm}^{-1}$  and  $2500\text{ cm}^{-1}$  is assigned to the N-H stretching of aromatic amine and aromatic C-H stretching and at  $1911\text{ cm}^{-1}$  and  $1790\text{ cm}^{-1}$ , the peaks obtained are attributed to aromatic C-H bending and C-N stretching of quinoid, respectively.<sup>32,47</sup> The FTIR spectra of composites as shown in Fig. 1(g) and (h) show the presence of some characteristic peaks belonging to each individual material, providing evidence of the good elaboration of the composites  $\text{Ag}_2\text{S@NH}_2\text{-MIL-125(Ti)/PANI}$  and  $\text{Bi}_2\text{S}_3\text{@NH}_2\text{-MIL-125(Ti)/PANI}$ . More characterizations have been performed to confirm these results.

**3.1.2. XRD patterns.** The XRD patterns of  $\text{NH}_2\text{-MIL-125(Ti)}$ ,  $\text{Ag}_2\text{S}$ ,  $\text{Bi}_2\text{S}_3$ ,  $\text{Ag}_2\text{S@NH}_2\text{-MIL-125(Ti)}$ ,  $\text{Bi}_2\text{S}_3\text{@NH}_2\text{-MIL-125(Ti)}$ , PANI,  $\text{Ag}_2\text{S@NH}_2\text{-MIL-125(Ti)/PANI}$ , and  $\text{Bi}_2\text{S}_3\text{@NH}_2\text{-MIL-125(Ti)/PANI}$  are shown in Fig. 2. It can be seen that the powder XRD patterns of the porous amino-functionalized titanium-based MOF,  $\text{NH}_2\text{-MIL-125(Ti)}$  and its successive modifications with  $\text{Ag}_2\text{S}$ ,  $\text{Bi}_2\text{S}_3$ , and PANI exhibit the same profile. The diffractogram of the synthesized  $\text{NH}_2\text{-MIL-125(Ti)}$  (a) presents remarkable characteristic peaks at  $2\theta$  ranging from  $5^\circ$  to  $25^\circ$ , which are in perfect agreement with the reported work.<sup>45–52</sup> This clearly shows that the precursor  $\text{NH}_2\text{-MIL-125(Ti)}$  sample at room temperature is a highly crystalline structure, and the main peaks appearing at  $6.7^\circ$ ,  $9.7^\circ$  and  $11.6^\circ$  match those of the simulated structure.<sup>41–44</sup> After loading with  $\text{Ag}_2\text{S}$  (b) and  $\text{Bi}_2\text{S}_3$  (c), the diffractograms of the resulting  $\text{Ag}_2\text{S@NH}_2\text{-MIL-125(Ti)}$  and  $\text{Bi}_2\text{S}_3\text{@NH}_2\text{-MIL-125(Ti)}$  labeled, respectively, as (d) and (e) clearly show that the crystalline structure of  $\text{NH}_2\text{-MIL-125(Ti)}$  is not affected, but the characteristic peaks for  $\text{Ag}_2\text{S}$  and  $\text{Bi}_2\text{S}_3$  are seen on it in the  $2\theta$  range from  $17^\circ$  to

$55^\circ$ , which are broad and weak probably due to their uniform dispersion. After adding PANI (f), the patterns recorded for  $\text{Ag}_2\text{S@NH}_2\text{-MIL-125(Ti)/PANI}$  (g) and  $\text{Bi}_2\text{S}_3\text{@NH}_2\text{-MIL-125(Ti)/PANI}$  (h) exhibit well-crystallized structures, confirming the uniformity of the prepared composites.

**3.1.3. SEM images.** The morphologies, structures and composition of the different films  $\text{NH}_2\text{-MIL-125(Ti)}$ ,  $\text{Ag}_2\text{S}$ ,  $\text{Bi}_2\text{S}_3$ ,  $\text{Ag}_2\text{S@NH}_2\text{-MIL-125(Ti)}$ ,  $\text{Bi}_2\text{S}_3\text{@NH}_2\text{-MIL-125(Ti)}$ , PANI,  $\text{Ag}_2\text{S@NH}_2\text{-MIL-125(Ti)/PANI}$ , and  $\text{Bi}_2\text{S}_3\text{@NH}_2\text{-MIL-125(Ti)/PANI}$  were investigated using SEM-EDX and element distribution mapping techniques. As can be observed in Fig. 3(A), the SEM image (a) obtained for the  $\text{NH}_2\text{-MIL-125(Ti)}$  sample exclusively displays characteristic plate-shaped structures with pore sites. After incorporating  $\text{Ag}_2\text{S}$  (b) and  $\text{Bi}_2\text{S}_3$  (c), they are well incorporated in the pore sites of the MOF and can be clearly identified on its surface as shown in (d) and (e). The presence of PANI (f) with well dispersed granular morphology formed by the agglomeration of nanospheres with some scattered pores of nanometer dimensions can also be seen on the resulting composites (g) and (h), making them more compact and agglomerated. SEM-EDX measurement was further applied to explore the existence of Ti, Ag, Bi, S, and other elements on the surface composition of the different films as depicted in Fig. 3(B) for EDX mapping and Fig. SI-2 (ESI<sup>†</sup>) for EDX spectra. From Fig. 3(B), the mapping of the core-shells clearly shows the presence of all the expected elements, which is confirmed by the peaks assigned to Ti, Ag, Bi, and S with a uniform distribution, and other elements observed in the spectra in Fig. SI-2 (ESI<sup>†</sup>).

**3.1.4.  $\text{N}_2$  adsorption-desorption analysis.** In order to determine the surface area and pore size distribution of the synthesized  $\text{NH}_2\text{-MIL-125(Ti)}$ ,  $\text{Ag}_2\text{S@NH}_2\text{-MIL-125(Ti)}$  and  $\text{Bi}_2\text{S}_3\text{@NH}_2\text{-MIL-125(Ti)}$ , the  $\text{N}_2$  sorption based on the Brunauer-Emmett-Teller (BET) method has been performed. The  $\text{N}_2$  adsorption-desorption isotherms of the samples shown in Fig. 4(A) exhibited type I isotherms recorded at 77 K with no hysteresis, indicating a significant presence of both micropores and mesopores within the framework structure of the MOF.<sup>35–44,53–55</sup> The BET surface area of (a) was  $1085.27\text{ m}^2\text{ g}^{-1}$  which is comparable to the value reported<sup>35</sup> ( $1169\text{ m}^2\text{ g}^{-1}$ ). Moreover, this surface area decreases drastically to  $415.82\text{ m}^2\text{ g}^{-1}$  and  $372.52\text{ m}^2\text{ g}^{-1}$  after surface modification with  $\text{Ag}_2\text{S}$  and  $\text{Bi}_2\text{S}_3$ , respectively, and can be justified by the partial occupation of the micropores, mesopores and obstructed pores of the pristine MOF as shown in Fig. 4(A)-(d) and (e), proving the success of the synthesis of the two core-shells as supported by the SEM analysis. The total pore volume and micropore volume calculated by the Durbinin-Radushkevich theory and the maximum pore width calculated by the ratio of total pore volume to the specific surface area obtained from Fig. 4(B) are shown in Table SI-1 (ESI<sup>†</sup>) with other BET-related parameters, and it can be noticed that (b) has better porosity property than (c).

**3.1.5. TGA/DTG analysis.** The TGA/DTG profiles of  $\text{NH}_2\text{-MIL-125(Ti)}$ ,  $\text{Ag}_2\text{S@NH}_2\text{-MIL-125(Ti)}$  and  $\text{Bi}_2\text{S}_3\text{@NH}_2\text{-MIL-125(Ti)}$  are shown in Fig. 5. The weight losses are subdivided here in four stages. The weight losses in stage 1 from  $95^\circ\text{C}$  to  $110^\circ\text{C}$  for all the three materials (a, b, and c) corresponding to

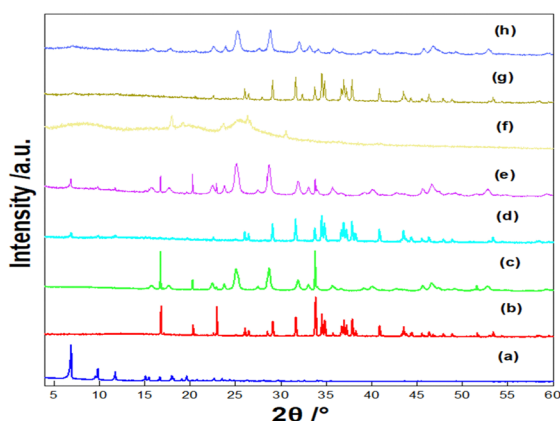
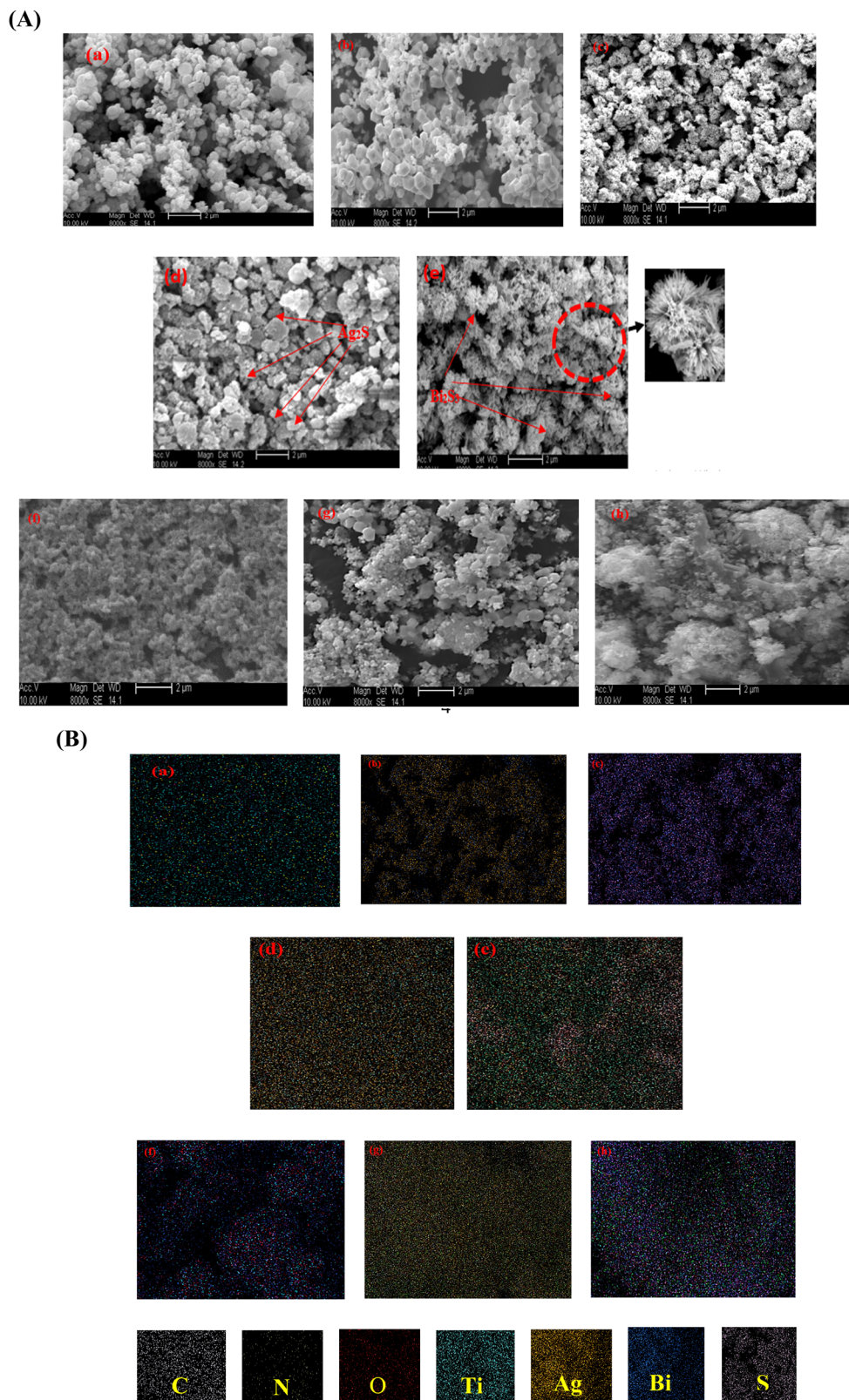


Fig. 2 XRD patterns of (a)  $\text{NH}_2\text{-MIL-125(Ti)}$ , (b)  $\text{Ag}_2\text{S}$ , (c)  $\text{Bi}_2\text{S}_3$ , (d)  $\text{Ag}_2\text{S@NH}_2\text{-MIL-125(Ti)}$ , (e)  $\text{Bi}_2\text{S}_3\text{@NH}_2\text{-MIL-125(Ti)}$ , (f) PANI, (g)  $\text{Ag}_2\text{S@NH}_2\text{-MIL-125(Ti)/PANI}$ , and (h)  $\text{Bi}_2\text{S}_3\text{@NH}_2\text{-MIL-125(Ti)/PANI}$ .







**Fig. 3** (A) SEM images and (B) EDX mapping of (a)  $\text{NH}_2\text{-MIL-125(Ti)}$ , (b)  $\text{Ag}_2\text{S}$ , (c)  $\text{Bi}_2\text{S}_3$ , (d)  $\text{Ag}_2\text{S}@ \text{NH}_2\text{-MIL-125(Ti)}$ , (e)  $\text{Bi}_2\text{S}_3@ \text{NH}_2\text{-MIL-125(Ti)}$ , (f) PANI, (g)  $\text{Ag}_2\text{S}@ \text{NH}_2\text{-MIL-125(Ti)}/\text{PANI}$ , and (h)  $\text{Bi}_2\text{S}_3@ \text{NH}_2\text{-MIL-125(Ti)}/\text{PANI}$ .

the loss of mass of about 30% in (a), 18% in (b) and 14% in (c) are assigned to the loss of MeOH and DMF from the pore as

well as the surface absorbed moisture ( $\text{H}_2\text{O}$ ) which was used to wash the MOF after synthesis. In stage 2, from 180 °C to 280 °C,

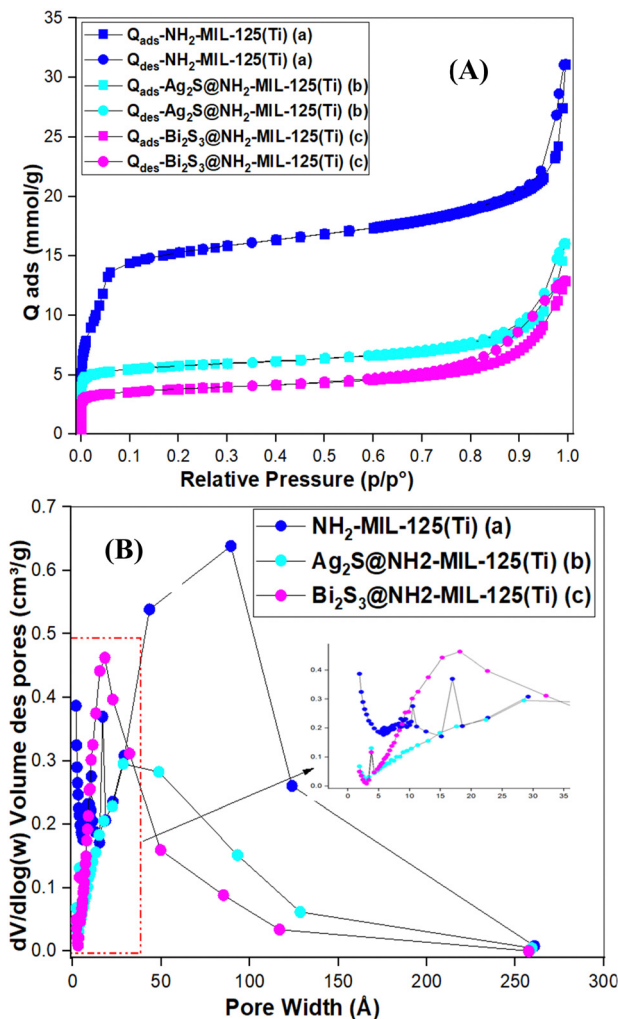


Fig. 4 (A) N<sub>2</sub> adsorption-desorption isotherms and (B) pore size distribution of (a) NH<sub>2</sub>-MIL-125(Ti), (b) Ag<sub>2</sub>S@NH<sub>2</sub>-MIL-125(Ti), and (c) Bi<sub>2</sub>S<sub>3</sub>@NH<sub>2</sub>-MIL-125(Ti).

the weight losses of 3% and 6% attributed, respectively, to the disintegration of Ag<sub>2</sub>S and Bi<sub>2</sub>S<sub>3</sub> at the surface of the two core-shells (b and c) are observed, where no mass loss is observed in that temperature range in (a), proving once more the successful preparation of the core-shells. In stage 3, around 290 °C up to 430 °C, major weight losses of about 42% in (a), 45% in (b), and 30% in (c) are attributed to the decomposition and oxidation of organic linkers of the framework constituents, accompanied with the formation of metal oxide particles and non-volatile macromolecular carbonaceous species, such as CO<sub>2</sub>, NO<sub>2</sub>, NO, NH<sub>3</sub> and H<sub>2</sub>O.<sup>44</sup> In stage 4, from 490 °C to 500 °C, a loss of mass of 4% appearing only on the curve of (a) is assigned to the disintegration of small amount of non-volatile macromolecular carbonaceous species and above that 500 °C, only TiO<sub>2</sub> is left as a residue on the three TGA/DTG profiles.<sup>44–52,56</sup>

### 3.2. Electrochemical characterization of the bare and modified GCEs

After the physicochemical characterization, the electrochemical characterization was performed using the potentiostat

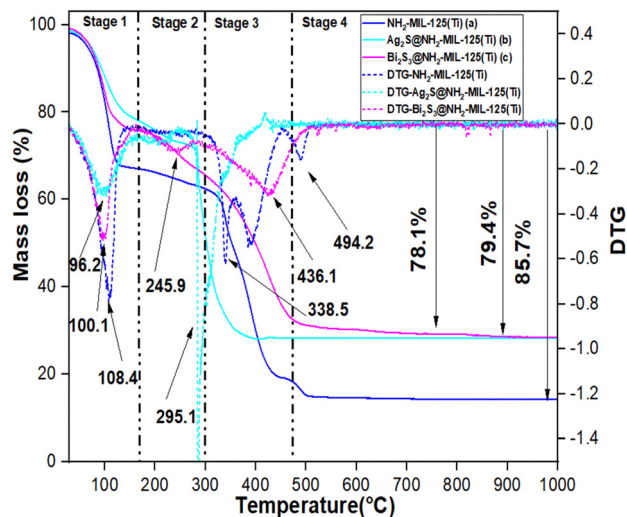


Fig. 5 TGA/DTG profiles of (a) NH<sub>2</sub>-MIL-125(Ti), (b) Ag<sub>2</sub>S@NH<sub>2</sub>-MIL-125(Ti) and (c) Bi<sub>2</sub>S<sub>3</sub>@NH<sub>2</sub>-MIL-125(Ti).

palmSens. In order to evaluate the permeability and conductivity of the prepared materials, the GCE modified with the thin film of each material was run inside 5 mM [Fe(CN)<sub>6</sub>]<sup>3-/4-</sup> in 0.1 M KCl (pH 7.0) using CV and EIS techniques. The intensity of the different peak currents obtained as shown in Fig. 6(A) follows the order  $h > i > g > e > f > d > a > b > c$ , while the values of charge transfer resistance (values given in bracket in Ohm) shown in Fig. 6(B) follow the order  $c (3264.85) > b (2768.73) > a (1913.44) > d (1340.97) > f (529.08) > e (479.92) > g (272.90) > i (38.16) > h (19.96)$ . The highest values of the peak current obtained with Ag<sub>2</sub>S@NH<sub>2</sub>-MIL-125(Ti)/PANI/GCE (h) and Bi<sub>2</sub>S<sub>3</sub>@NH<sub>2</sub>-MIL-125(Ti)/PANI/GCE (i) which are, respectively, 3.78 and 2.31 times higher than the one obtained with bare GCE (a) can be explained by the synergistic effects of Ag<sub>2</sub>S, Bi<sub>2</sub>S<sub>3</sub>, NH<sub>2</sub>-MIL-125(Ti), and PANI, which are related respectively to their electrocatalytic ability, porosity, conductivity, and large specific surface area. The corresponding  $R_{ct}$  values determined by the extrapolation of the semi-cycle of the Nyquist curves have shown that Ag<sub>2</sub>S@NH<sub>2</sub>-MIL-125(Ti)/PANI/GCE (h) and Bi<sub>2</sub>S<sub>3</sub>@NH<sub>2</sub>-MIL-125(Ti)/PANI/GCE allow the passage of electrons respectively 95.84 and 50.14 times faster than the bare GCE.

The active surfaces of the bare GCE, Ag<sub>2</sub>S@NH<sub>2</sub>-MIL-125(Ti)/PANI/GCE, and Bi<sub>2</sub>S<sub>3</sub>@NH<sub>2</sub>-MIL-125(Ti)/PANI/GCE were found to be 0.0029 cm<sup>2</sup>, 0.0095 cm<sup>2</sup>, and 0.0062 cm<sup>2</sup>, respectively, obtained from the Randles Sevcik equation<sup>32,36,57,58</sup> as shown in SI-6 (ESI<sup>†</sup>).

### 3.3. Electrochemical sensing of uric acid

Prior to using each fabricated electrode for the electroanalysis of uric acid (UA), they were stabilized in a solution of 0.10 M phosphate buffer at pH 7.0, by running multicyclic voltammograms and it was found that maximum 6 cycles shown in Fig. SI-4 (ESI<sup>†</sup>) were sufficient to stabilize the working electrodes.

**3.3.1. Behaviour of UA, influence of the modification of the bare GCE and kinetic studies.** The electrochemical behaviour of





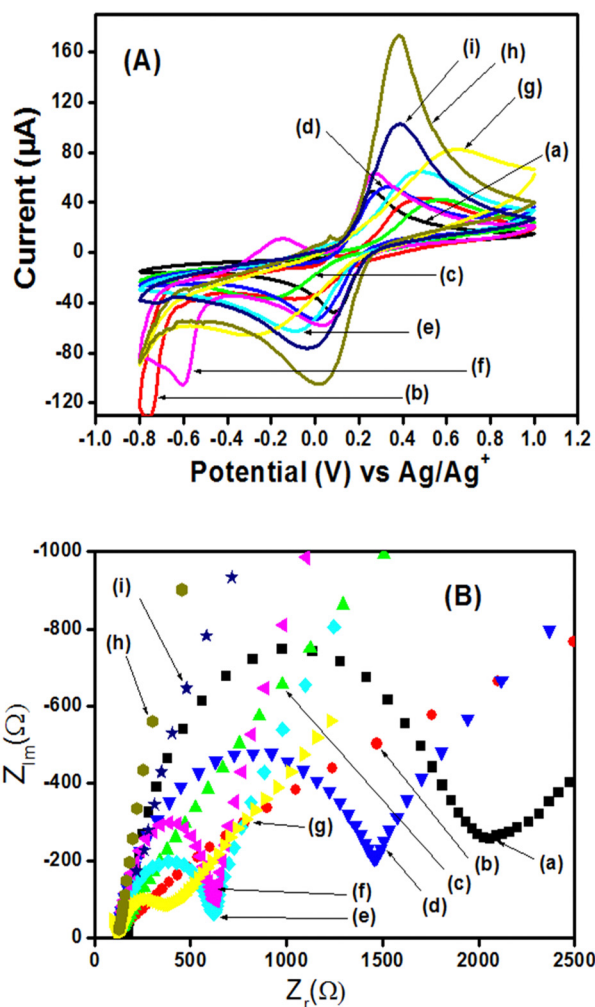


Fig. 6 (A) Cyclic voltammograms of 5 mM  $[\text{Fe}(\text{CN})_6]^{3-/4-}$  (0.10 M KCl, pH 7) recorded on the different electrodes: bare GCE (a),  $\text{Ag}_2\text{S}/\text{GCE}$  (b),  $\text{Bi}_2\text{S}_3/\text{GCE}$  (c),  $\text{NH}_2\text{-MIL-125}(\text{Ti})/\text{GCE}$  (d),  $\text{Ag}_2\text{S}@ \text{NH}_2\text{-MIL-125}(\text{Ti})/\text{GCE}$  (e),  $\text{Bi}_2\text{S}_3@ \text{NH}_2\text{-MIL-125}(\text{Ti})/\text{GCE}$  (f),  $\text{PANI}/\text{GCE}$  (g),  $\text{Ag}_2\text{S}@ \text{NH}_2\text{-MIL-125}(\text{Ti})/\text{PANI}/\text{GCE}$  (h), and  $\text{Bi}_2\text{S}_3@ \text{NH}_2\text{-MIL-125}(\text{Ti})/\text{PANI}/\text{GCE}$  (i). Scan rate =  $50 \text{ mV s}^{-1}$ . (B) Electrochemical impedance spectra obtained under the same conditions as in cyclic voltammetry with the same electrodes.

1 mM UA (0.10 M PB, pH 7.0) was investigated *via* cyclic voltammetry (CV), while the influence of the modification was determined using  $50 \mu\text{M}$  UA (0.10 M PB, pH 7.0) *via* differential pulse voltammetry (DPV) with a bare and modified GCE. The cyclic voltammograms obtained as shown in Fig. 7(A) were recorded in the potential range from 0.0 V to 0.80 V at a scan rate of  $50 \text{ mV s}^{-1}$  and it can be concluded that UA has a single oxidation peak, which is irreversible at the surface of electrodes.

The voltammograms shown in Fig. 7(B) were obtained between 0.0 V and 0.70 V. The highest peak current values obtained with  $\text{Ag}_2\text{S}@ \text{NH}_2\text{-MIL-125}(\text{Ti})/\text{PANI}/\text{GCE}$  and  $\text{Bi}_2\text{S}_3@ \text{NH}_2\text{-MIL-125}(\text{Ti})/\text{PANI}/\text{GCE}$  are respectively 2.45 and 2.31 times higher than the one obtained with the bare GCE as shown in the inset histogram (Fig. 7(C)). These results can be explained by the good synergetic effect generated from the combination of the core-

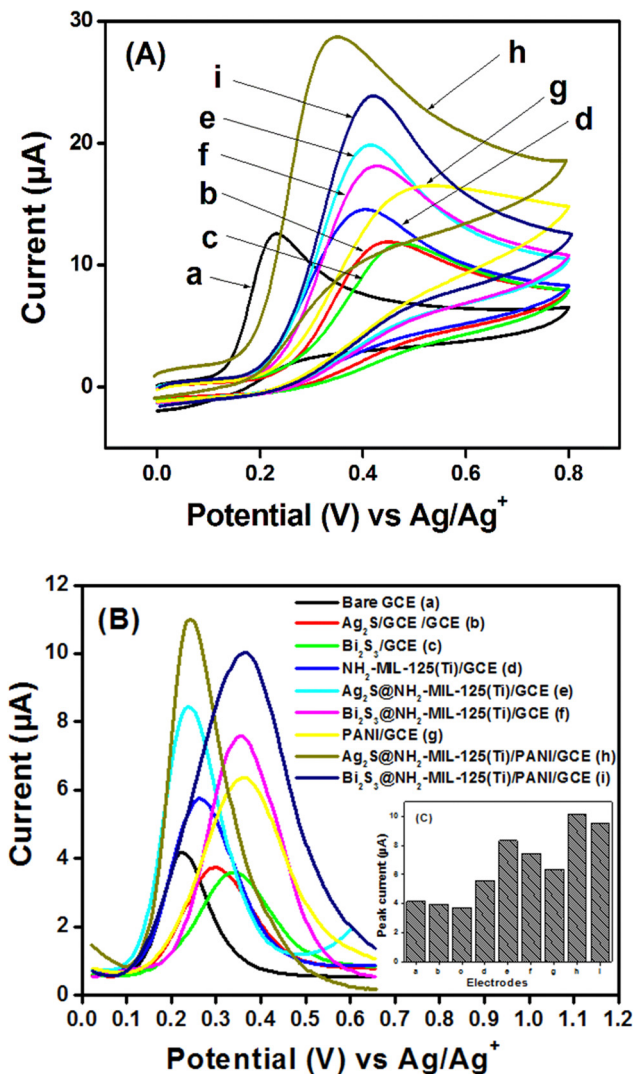


Fig. 7 (A) Cyclic voltammograms (1 mM UA) and (B) of differential pulse voltammograms ( $50 \mu\text{M}$  UA) recorded in 0.10 M phosphate buffer solution, at pH 7, using: Bare GCE (a),  $\text{Ag}_2\text{S}/\text{GCE}$  (b),  $\text{Bi}_2\text{S}_3/\text{GCE}$  (c),  $\text{NH}_2\text{-MIL-125}(\text{Ti})/\text{GCE}$  (d),  $\text{Ag}_2\text{S}@ \text{NH}_2\text{-MIL-125}(\text{Ti})/\text{GCE}$  (e),  $\text{Bi}_2\text{S}_3@ \text{NH}_2\text{-MIL-125}(\text{Ti})/\text{GCE}$  (f),  $\text{PANI}/\text{GCE}$  (g),  $\text{Ag}_2\text{S}@ \text{NH}_2\text{-MIL-125}(\text{Ti})/\text{PANI}/\text{GCE}$  (h), and  $\text{Bi}_2\text{S}_3@ \text{NH}_2\text{-MIL-125}(\text{Ti})/\text{PANI}/\text{GCE}$  (i). (C) Inset shows the corresponding histogram. Scan rate =  $50 \text{ mV s}^{-1}$ .

shells with a metal-organic framework and polyaniline. It can be noticed that the oxidation peak obtained with  $\text{Ag}_2\text{S}@$  has more electrocatalytic effect than  $\text{Bi}_2\text{S}_3@$ , which is surely assigned to the fact that Ag has less weight than Bi. The types of interaction which may occur at the surface of the modified electrode have been illustrated in Scheme SI-1 (ESI $^\dagger$ ).

The kinetic studies have been evaluated at different scan rates in the scanning range from 10 to  $150 \text{ mV s}^{-1}$ , as shown in Fig. SI-5 (ESI $^\dagger$ ). The plotting of the peak current *versus* the root square of the scan rate shows the correlation coefficient values (0.999 for  $\text{Ag}_2\text{S}@$  and 0.996 for  $\text{Bi}_2\text{S}_3@$ ) closed to 1, indicating that diffusion is the phenomenon which governs the transfer of particles at the surface of electrodes. Other kinetic parameters are given in SI-8 (ESI $^\dagger$ ).



**3.3.2. Influence of pH and accumulation time.** The influence of pH of the study medium has been observed in the range from 2 to 10 using the two modified electrodes  $\text{Ag}_2\text{S@NH}_2\text{-MIL-125(Ti)/PANI/GCE}$  and  $\text{Bi}_2\text{S}_3\text{@NH}_2\text{-MIL-125(Ti)/PANI/GCE}$  and the voltammograms obtained are shown respectively in Fig. 8(A) and (B). It is observed that the peak current increase up to 7 and decrease till pH 10 are shown in Fig. 8(C-1) and (D-1), respectively. The peak potential was found to decrease linearly with the increase of pH as shown in Fig. 8(C-2) and (D-2). The lowest peak current obtained in acid medium may be due to the poor affinity between the modified electrodes and uric acid, and also due to the electrostatic repulsion that occurs between the materials charged positively with the protonation of the  $-\text{NH}_2$  function of the MOF to form  $-\text{NH}_3^+$  and UA charged positively in a low acidic medium.<sup>59</sup> Less solubility of UA in an acid range makes particles difficult to diffuse at the surface of electrodes, which may also justify the lowest peaks obtained in an acid medium. The change of the potential with the pH is the proof that this analysis is protons-dependent. The resulting linear equations gave slopes of  $-0.078$  and  $-0.062$  for the  $\text{Ag}_2\text{S@}$ - and  $\text{Bi}_2\text{S}_3\text{@}$ - electrodes, respectively, which implies that the number of electrons exchanged during the oxidation of UA using the two modified electrodes is equal to the number of protons consumed, that is, one electron-one proton exchange as shown during the kinetic study.

It is clearly seen in Fig. SI-6A and B ( $\text{ESI}^\dagger$ ) that the peak current rapidly increases with the accumulation time up to 2 min and gets stabilized respectively for  $\text{Ag}_2\text{S@}$ - and  $\text{Bi}_2\text{S}_3\text{@}$ -sensors. This increase can be explained by the large availability of the active surface areas and porosity sites, which get saturated after 2 min due to the total occupation of the fixation sites of the film by uric acid molecules. Therefore, pH 7.0 and accumulation time of 2 min (120 s) have been used as optimal parameters for the study of influence of concentration in the phosphate buffer solution.

**3.3.3. Influence of concentration.** The determination of the limit of detection (LOD) below the physiological reference range at pH 7.0 was done by varying the concentration of UA from 1 to 16  $\mu\text{M}$ , and the responses obtained with the modified electrodes are given by the voltammograms shown in Fig. 9(A) and (B). The calibration curves were plotted and good linearity was obtained (Fig. 9(C) and (D)) and they were then used to calculate the LOD ( $3\text{Sb}/m$ ), with Sb being the error on the blank and  $m$  being the slope.<sup>60</sup> The sensitivities and LOD obtained with the sensor  $\text{Ag}_2\text{S@NH}_2\text{-MIL-125(Ti)/PANI/GCE}$  are  $299 \mu\text{A mM}^{-1}$  and  $5.789 \times 10^{-7} \text{ M}$ , while with the sensor  $\text{Bi}_2\text{S}_3\text{@NH}_2\text{-MIL-125(Ti)/PANI/GCE}$ , they are  $263 \mu\text{A mM}^{-1}$  and  $4.463 \times 10^{-7} \text{ M}$  respectively. Therefore, it can be concluded that  $\text{Ag}_2\text{S@}$ - has higher sensitivity, but the better limit of detection is obtained with  $\text{Bi}_2\text{S}_3\text{@}$ -. The comparison of the LOD obtained in this work with those obtained in the other reported works is shown in Table 1, which clearly shows that our LOD values are comparable to the ones reported in recent literature. Moreover, those values of LODs are much lower than the physiological reference range of UA (160–500  $\mu\text{M}$ ), which means that the proposed sensors can be used effectively for the sensing of UA in real media.

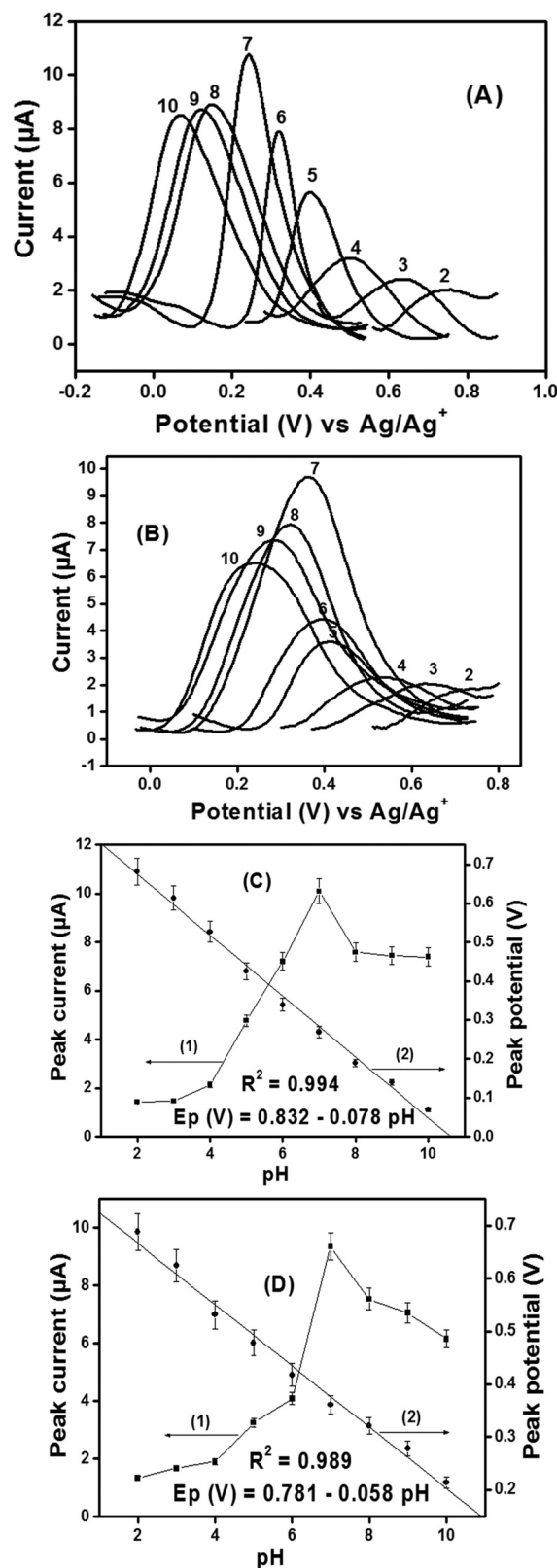


Fig. 8 Effect of pH on differential pulse voltammograms of UA using  $\text{Ag}_2\text{S@NH}_2\text{-MIL-125(Ti)/PANI/GCE}$  (A) and  $\text{Bi}_2\text{S}_3\text{@NH}_2\text{-MIL-125(Ti)/PANI/GCE}$  (B). The oxidation peak currents (C-1) and (D-1) and oxidation peak potentials (C-2) and (D-2) obtained are shown, respectively. Experimental conditions: 50  $\mu\text{M}$  UA in 0.1 M phosphate buffer solution with pH values of 2, 3, 4, 5, 6, 7, 8, 9 and 10. Experiments were conducted in triplicate.

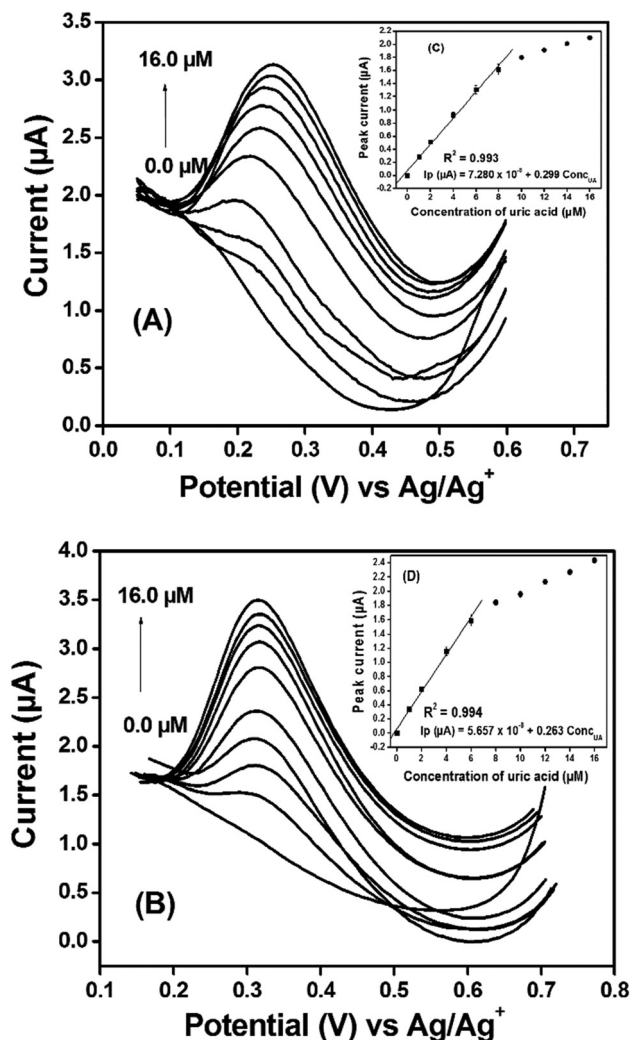


Fig. 9 Differential pulse voltammograms of uric acid (0, 1, 2, 4, 6, 8, 10, 12, 14, and 16 μM) in the phosphate buffer solution (0.10 M, pH 7) using Ag<sub>2</sub>S@NH<sub>2</sub>-MIL-125(Ti)/PANI/GCE (A) and Bi<sub>2</sub>S<sub>3</sub>@NH<sub>2</sub>-MIL-125(Ti)/PANI/GCE (B). The insets (C) and (D) show the corresponding calibration curves. 2 min of accumulation. Experiments were conducted in triplicate.

**3.3.4. Interference study, reproducibility, repeatability, and stability of the modified electrode.** The selectivity of the sensors has been evaluated *via* chronoamperometry (Fig. SI-7, ESI<sup>†</sup>), which is an appropriate method for the simultaneous study of the effect of several compounds in the presence of the target compounds and it was found that ascorbic acid, tartrazine and adrenaline can interfere with the signal of UA when using Ag<sub>2</sub>S@-, while adrenaline, tyrosine, and butylated hydroxyanisole can interfere with the signal of UA when using Bi<sub>2</sub>S<sub>3</sub>@-. These results reveal that the developed sensors, apart from being used for the sensing of UA, can also be used for the sensing of adrenaline as it interfered with the two electrodes.

The reproducibility of the sensors has been evaluated by recording nine successive measurements on the same films and the DPV responses are shown in Fig. SI-8A and B (ESI<sup>†</sup>), and the repeatability was assessed by recording the signal of nine successive film preparations and the results are shown in

Table 1 Comparison of the analytical performance of other modified electrodes in the literature reports

Electrode	Methods	Linear range (μM)	LOD (μM)	Ref.
HNGA/GCE	DPV	5–50	0.12	27
GQDs/IL-SPCE	DPV	0.5–20	0.03	19
ERGO/GCE	DPV	0.5–60	0.5	61
Au/rGO/GCE	DPV	8.8–53	1.8	62
Chitosan-graphene	DPV	2.0–45	2	63
G-30	SWV	0.5–150	0.29	64
PBG/GCE	DPV	0.5–200	0.17	65
3DGH-Fc/GCE	DPV	8–400	0.07	66
GO-PANI/GCE	DPV	3–26	1	67
ZIF-11/GCE	DP-ASV	20–540	0.48	68
Nano-CaCO <sub>3</sub> /PANI/rGO/GCE	DPV	0.1–60	0.04	32
ERp-NBA/GO/CPE	DPV	0.1–600	0.05	69
Ag <sub>2</sub> S@NH <sub>2</sub> -MIL-125(Ti)/PANI/GCE	DPV	1–16	0.58	This work
Bi <sub>2</sub> S <sub>3</sub> @NH <sub>2</sub> -MIL-125(Ti)/PANI/GCE	DPV	1–16	0.45	This work

DPV: Differential pulse voltammetry; SWV: square wave voltammetry; DP-ASV: differential pulse–anodic stripping voltammetry; HNGA/GCE: holey nitrogen-doped graphene aerogel; GQDs/IL-SPCE: graphene quantum dots/ionic liquid modified screen-printed carbon electrode; ERGO/GCE: electrochemically reduced graphene oxide modified glassy carbon electrode; Au/rGO/GCE: reduced graphene oxide and Au nanoplates modified glassy carbon electrode; G-30: graphene ink; PBG/GCE: poly(bromocresol green) modified glassy carbon electrode; DGH-Fc/GCE: ferrocene hybrid (Fc)/three dimensional graphene hydrogel (3DGH) nanocomposite modified glassy carbon electrode; ZIF-11/GCE: zeolite imidazolate framework-11 modified glassy carbon electrode; GO-PANI/GCE: graphene oxide-templated polyaniline microspheres modified glassy carbon electrode; nano-CaCO<sub>3</sub>/PANI/rGO/GCE: glassy carbon electrode modified with reduced graphene oxide, polyaniline, and nano-calcium carbonate; ERp-NBA/GO/CPE: carbon paste electrode modified with an electrochemically reduced *para*-nitrobenzoic acid/graphene oxide nanocomposite.

Fig. SI-8C and D (ESI<sup>†</sup>), while the storage stability was evaluated by recording the DPV signal of the prepared electrodes once per week during five weeks (Fig. SI-8E and F, ESI<sup>†</sup>) respectively for Ag<sub>2</sub>S@NH<sub>2</sub>-MIL-125(Ti)/PANI/GCE and Bi<sub>2</sub>S<sub>3</sub>@NH<sub>2</sub>-MIL-125(Ti)/PANI/GCE. The results show that the prepared sensors have good reproducibility (recovery of  $98.51 \pm 0.95$  and  $95.76 \pm 2.10$ ), repeatability (recovery of  $100.05 \pm 0.08$  and  $96.56 \pm 1.76$ ), and stability (recovery of  $97.27 \pm 0.11$  and  $99.20 \pm 0.003$ ) respectively for Ag<sub>2</sub>S@- and Bi<sub>2</sub>S<sub>3</sub>@-.

**3.3.5. Real medium.** Two human urine samples (US1 and US2) in which 1 mL was taken and diluted 200 times with PB (pH 7.0, 0.10 M) were chosen as the actual samples to investigate the possibility of the application of the proposed method. After centrifugation (4000 rpm, 10 min), the standard addition technique was utilized to measure the recovery using the proposed DPV method, and the corresponding voltammograms are shown in Fig. 10. The summarized results for the analysis of US are given in Table 2. The recovery of the proposed method is accurate and precise, indicating that Ag<sub>2</sub>S@NH<sub>2</sub>-MIL-125(Ti)/PANI/GCE and Bi<sub>2</sub>S<sub>3</sub>@NH<sub>2</sub>-MIL-125(Ti)/PANI/GCE may be efficiently used for the elaboration of the point-of-care testing device for the determination of UA in urine samples.

## 4. Conclusion

The aim of this study was to develop and compare the capacity of two core-shell sensors based on metal-organic frameworks



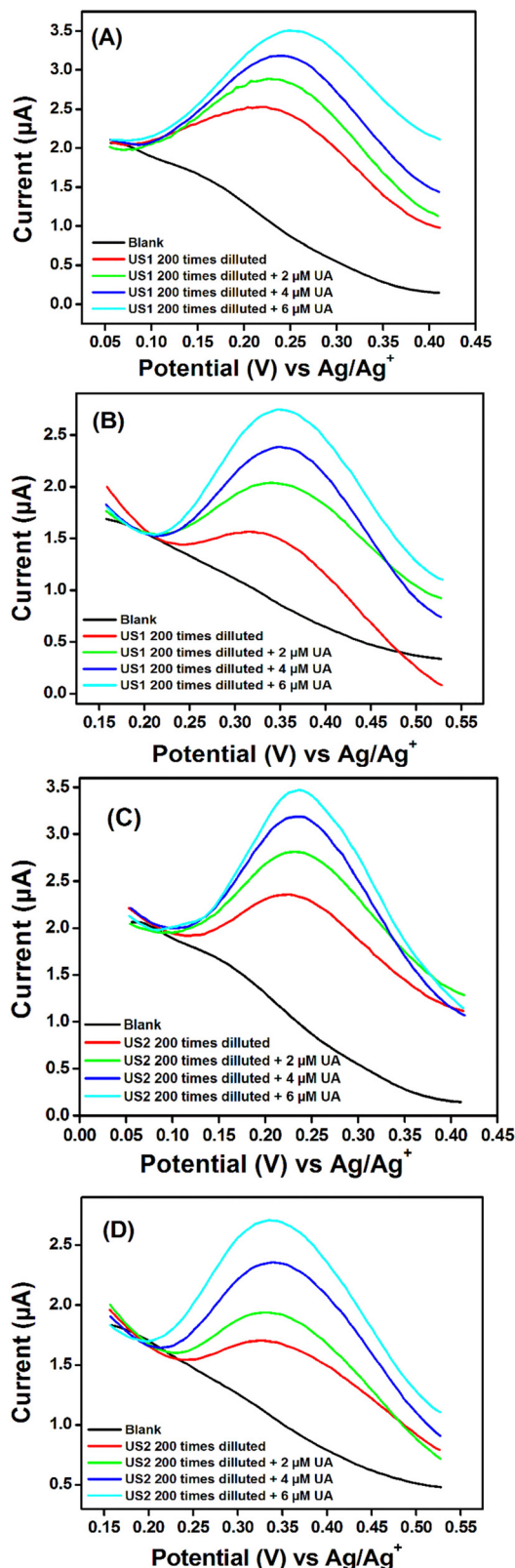


Fig. 10 Differential pulse voltammograms of two human urine samples (US1 and US2) analyzed using  $\text{Ag}_2\text{S}@\text{NH}_2\text{-MIL-125(Ti)/PANI/GCE}$  (A), (C) and  $\text{Bi}_2\text{S}_3@\text{NH}_2\text{-MIL-125(Ti)/PANI/GCE}$  (B), (D) in which the urine samples were diluted 200 times with PB (pH 7.0, 0.10 M) and spiked with 0, 2, 4, and 6  $\mu\text{M}$  UA, respectively.

Table 2 Determination of UA in two human urine samples ( $n = 3$ )

Electrode	Analyte	detected ( $\mu\text{M}$ )	Spiked ( $\mu\text{M}$ )	Found ( $\mu\text{M}$ )	Recovery (%)	RSD
$\text{Ag}_2\text{S}@\text{NH}_2\text{-MIL-125(Ti)/PANI/GCE}$	US1	1.37	2	3.23	95.85	1.45
			4	5.20	96.78	
			6	7.29	98.70	
	US2	1.03	2	3.17	104.35	4.03
			4	5.07	100.66	
			6	6.77	96.30	
$\text{Bi}_2\text{S}_3@\text{NH}_2\text{-MIL-125(Ti)/PANI/GCE}$	US1	0.85	2	2.89	101.44	3.49
			4	4.63	95.44	
			6	6.53	95.36	
	US2	0.68	2	2.57	95.71	3.33
			4	4.72	100.75	
			6	6.81	102.01	

Recovery = found/(spiked + detected)  $\times$  100; RSD = relative standard deviation from the three spiked; ND = non determined.

(MOFs) and polyaniline (PANI) for the determination of a pathological analyte, uric acid (UA), in aqueous solution and urine samples. Accordingly, two sensors have been developed by preparing two composites of core-shells@MOF and PANI with 5% gelatin as the binder. After their immobilization on the glassy carbon electrode (GCE),  $\text{Ag}_2\text{S}@\text{NH}_2\text{-MIL-125(Ti)/PANI/GCE}$  and  $\text{Bi}_2\text{S}_3@\text{NH}_2\text{-MIL-125(Ti)/PANI/GCE}$  were then obtained as working electrodes. Prior to that, the individual and composite materials were characterized using physico-chemical and electro-chemical techniques, showing the success of the synthesis with resulting good porosities and crystallinities, large specific surface areas, good thermal stabilities, low charge transfer resistance, *etc.* The fabricated sensors exhibited high sensitivity toward the electro-oxidation of UA over a calibration range from 0 to 16  $\mu\text{M}$ , leading to higher sensitivities and limits of detection (LODs). The sensors showed good reproducibility, repeatability, stability, excellent selectivity, and were applied to analyze two human urine samples after dilution and spiking. The sensors were able to detect UA in urine samples even after 200 times of dilution. Finally, through the entire work, the sensor  $\text{Ag}_2\text{S}@\text{NH}_2\text{-MIL-125(Ti)/PANI/GCE}$  shows more promising results for the development of point-of-care devices than the sensor  $\text{Bi}_2\text{S}_3@\text{NH}_2\text{-MIL-125(Ti)/PANI/GCE}$  with a few exceptions in certain parameters.

## Author contributions

Gullit Deffo: conceptualization, formal analysis, methodology, investigation, writing original draft. Cyrille Ghislain Fotsop: S conceptualization, synthesis, characterizations, editing. Marcel Cédric Deussi Ngaha: methodology, editing, review. Sengor Gabou Fogang: formal analysis, investigation. Lionnel Averie Vomo: methodology, investigation. Bibiane Wandji Nkuigoua: methodology, investigation. Akenmo Shella: methodology, investigation. Alex Vincent Somba: review, editing. Thierry Flavien Nde Tene: review, editing. Ida Kouam Tchummegne: review, editing. Evangéline Njanja: review, validation, supervision. Ignas Kenfack Tonlé: validation, supervision. Panchanan Puzari: methodology, review, editing, validation. Emmanuel Ngameni: supervision, project administration.





## Conflicts of interest

There are no conflicts to declare.

## Acknowledgements

Dr Gullit DEFFO thanks DBT-TWAS for the fellowship DBT-TWAS Sandwich Postgraduate Fellowship (2019, FR number: 3240313785) and the contribution of the Alexander von Humboldt Foundation (AvH), the German Ministry for Economic Cooperation and Development (BMZ) and the African-German Network of Excellence in Science (AGNES, 2023). Mr Cyrille G. Fotsop thanks the German Academic Exchange Service (DAAD) for their financial support (FR number: 57588366). The authors also thank the volunteers who provided the urine samples for analysis.

## References

- 1 Y. Dai and C. C. Liu, Recent Advances on Electrochemical Biosensing Strategies toward Universal Point-of-Care Systems, *Angew. Chem.*, 2019, **58**, 12355–12368.
- 2 J. Wang, Electrochemical Biosensors: Towards Point-of-Care cancer diagnostics, *Biosens. Bioelectron.*, 2006, **21**, 1887–1892.
- 3 A. S. John and C. P. Price, Existing and Emerging Technologies for Point-of-Care Testing, *Clin. Biochem.*, 2014, **35**, 155–167.
- 4 L. Fraisse, M. C. Bonnet, J. P. de Farcy, C. Agut, D. Dersigny and A. Bayol, A colorimetric 96-well microtiter plate assay for the determination of urate oxidase activity and its kinetic parameters, *Anal. Biochem.*, 2002, **309**, 173–179.
- 5 D. Jin, M. H. Seo, B. T. Huy, Q. T. Pham, M. L. Conte, D. Thangadurai and Y. I. Lee, Quantitative determination of Uric Acid Using CdTe Nanoparticles as Fluorescence Probes, *Biosens. Bioelectron.*, 2016, **77**, 359–365.
- 6 X. Dai, X. Fang, C. Zhang, R. Xu and B. Xu, Determination of serum uric acid using high-performance liquid chromatography (HPLC)/isotope dilution mass spectrometry (ID-MS) as a candidate reference method, *J. Chromatogr. B: Anal. Technol. Biomed. Life Sci.*, 2007, **857**, 287–295.
- 7 Q. Li, S. Wei, D. Wu, C. Wen and J. Zhou, Urinary Metabolomics Study of Patients with Gout Using Gas Chromatography-Mass Spectrometry, *BioMed Res. Int.*, 2018, **2018**, 1–10.
- 8 S. K. Maji, A. K. Mandal, K. T. Nguyen, P. Borah and Y. Zhao, Cancer cell detection and therapeutics using peroxidase-active nanohybrid of gold nanoparticle-loaded mesoporous silica-coated graphene, *ACS Appl. Mater. Interfaces*, 2015, **7**, 9807–9816.
- 9 S. Zhao, J. Wang, F. Ye and Y. M. Liu, Determination of Uric Acid in Human Urine and Serum by Capillary Electrophoresis with Chemiluminescence Detection, *Anal. Biochem.*, 2008, **378**, 127–131.
- 10 S. R. Maxwell, H. Thomason, D. Sandler, C. Leguen, M. A. Baxter, G. H. Thorpe, A. F. Jones and A. H. Barnett, Antioxidant Status in Patients with Uncomplicated Insulin-Dependent and Non-Insulin-Dependent Diabetes Mellitus, *Eur. J. Clin. Invest.*, 1997, **27**, 484–490.
- 11 B. N. Ames, R. Cathcart, E. Schwiers and P. Hochstein, Uric Acid Provides an Antioxidant Defense in Humans against Oxidant- and Radical-Caused Aging and Cancer: A Hypothesis, *Proc. Natl. Acad. Sci. U. S. A.*, 1981, **78**, 6858–6862.
- 12 J. Liu, C. Xu, L. Ying, S. Zang, Z. Zhuang, H. Lv, W. Yang, Y. Luo, X. Ma, L. Wang, Y. Xun, D. Ye and J. Shi, Relationship of Serum Uric Acid Level with Non-Alcoholic Fatty Liver Disease and Its Inflammation Progression in Non-Obese Adults, *Hepatol. Res.*, 2017, **47**, E104–E112.
- 13 M. T. Pellecchia, R. Savastano, M. Moccia, M. Picillo, P. Siano, R. Erro, A. Vallelunga, M. Amboni, C. Vitale, G. Santangelo and P. Barone, Lower Serum Uric Acid Is Associated with Mild Cognitive Impairment in Early Parkinson's Disease: A 4-Year Follow-up Study, *J. Neural Transm.*, 2016, **123**, 1399–1402.
- 14 Y. Kubota, M. McAdams-DeMarco and A. R. Folsom, Serum Uric Acid, Gout, and Venous Thromboembolism: The Atherosclerosis Risk in Communities Study, *Thromb. Res.*, 2016, **144**, 144–148.
- 15 K. Arora, M. Tomar and V. Gupta, Highly sensitive and selective uric acid biosensor based on RF sputtered NiO thin film, *Biosens. Bioelectron.*, 2011, **30**, 333–336.
- 16 W. L. Nyhan, The recognition of Lesch-Nyhan syndrome as an inborn error of purine metabolism, *J. Inherited Metab. Dis.*, 1997, **20**, 171–178.
- 17 F. C. Martin, J. T. Suarez, H. G. Acosta, C. Aparicio, M. L. J. Roldan, B. Stiburkova, K. Ichida, M. A. M. Gomez, M. H. Goni, M. C. H. Barquero, V. Inigo, R. Enrique, E. C. Lanus, V. M. G. Nieto and R. T. Group, URAT1 and GLUT9 Mutations in Spanish Patients with Renal Hypouricemia, *Clin. Chim. Acta*, 2018, **481**, 83–89.
- 18 D. M. Vidanapathirana, S. Jayasena, E. Jasinge and B. Stiburkova, A Heterozygous Variant in the SLC22A12 gene in a Sri Lanka Family Associated with Mild Renal Hypouricemia, *BMC Pediatr.*, 2018, **18**, 1–5.
- 19 K. Kunpatee, S. Traipop, O. Chailapakul and S. Chuanuwatanakul, Simultaneous determination of ascorbic acid, dopamine, and uric acid using graphene quantum dots/ionic liquid modified screen-printed carbon electrode, *Sens. Actuators, B*, 2020, **314**, 128059.
- 20 S. Reddy, B. E. K. Swamy and H. Jayadevappa, CuO nanoparticle sensor for the electrochemical determination of dopamine CuO nanoparticle sensor for the electrochemical determination of dopamine, *Electrochim. Acta*, 2012, **61**, 78–86.
- 21 J. Huang, Y. Liu, H. Hou and T. You, Simultaneous Electrochemical determination of dopamine, uric acid and ascorbic acid using palladium nanoparticle -loaded carbon nanofiber modified electrode, *Biosens. Bioelectron.*, 2008, **24**, 632–637.
- 22 G. Deffo, R. Hazarika, M. C. D. Ngaha, M. Basumatary, S. Kalita, N. Hussain, E. Njanja, P. Puzari and E. Ngameni, Ultra-sensitive uric acid second generation biosensor based on chemical immobilization of uricase on functionalized



- multiwall carbon nanotube grafted palm oil fiber in the presence of ferrocene mediator, *Anal. Methods*, 2023, **15**, 2456–2466.
- 23 Y. Wu, P. Deng, Y. Tian, J. Feng, J. Xiao, J. Li, J. Liu, G. Li and Q. He, Simultaneous and sensitive determination of ascorbic acid, dopamine and uric acid via an electrochemical sensor based on PVP-graphene composite, *J. Nanobiotechnol.*, 2020, **18**, 1–13.
  - 24 Y. Wei, Y. Liu, Z. Xu, S. Wang, B. Chen, D. Zhang and Y. Fang, Simultaneous Detection of Ascorbic Acid, Dopamine, and Uric Acid Using a Novel Electrochemical Sensor Based on Palladium Nanoparticles/Reduced Graphene Oxide Nanocomposite, *Int. J. Anal. Chem.*, 2020, **2020**, 1–13.
  - 25 J. Feng, Q. Li, J. Cai, T. Yang, J. Chen and X. Hou, Electrochemical detection mechanism of dopamine and uric acid on titanium nitride-reduced graphene oxide composite with and without ascorbic acid, *Sens. Actuators, B*, 2019, **298**, 126872.
  - 26 L. Wang, R. Yang, L. Qu and P. B. Harrington, Electrostatic repulsion strategy for high-sensitive and selective determination of dopamine in the presence of uric acid and ascorbic acid, *Talanta*, 2020, **210**, 120626.
  - 27 S. Feng, L. Yu, M. Yan, J. Ye, J. Huang and X. Yang, Holey nitrogen-doped graphene aerogel for simultaneously electrochemical determination of ascorbic acid, dopamine and uric acid, *Talanta*, 2021, **224**, 121851.
  - 28 G. A. Tiğ, Development of electrochemical sensor for detection of ascorbic acid, dopamine, uric acid and l-tryptophan based on Ag nanoparticles and poly(L-arginine)-graphene oxide composite, *J. Electroanal. Chem.*, 2017, **807**, 19–28.
  - 29 T. A. Hassan, V. K. Rangari and S. Jeelani, Value-Added Biopolymer Nanocomposites from Waste EggshellBased CaCO<sub>3</sub> Nanoparticles as Fillers, *ACS Sustainable Chem. Eng.*, 2014, **2**, 706–717.
  - 30 Q. Ding, L. Cao, M. Liu, H. Lin and D. P. Yang, Au nanoparticle-loaded eggshell for electrochemical detection of nitrite, *RSC Adv.*, 2021, **11**, 4112–4117.
  - 31 S. F. D'Souza, J. Kumar, S. K. Jha and B. S. Kubal, Immobilization of the urease on eggshell membrane and its application in biosensor, *Mater. Sci. Eng.*, 2013, **33**, 850–854.
  - 32 G. Deffo, M. Basumatary, N. Hussain, R. Hazarika, S. Kalita, E. Njanja and P. Puzari, Eggshell nano-CaCO<sub>3</sub> decorated PANI/rGO composite for sensitive determination of ascorbic acid dopamine and uric acid in human blood serum and urine, *Mater. Today Commun.*, 2022, **33**, 104357.
  - 33 D. Botta, I. Enculescu, C. Balan and V. C. Diculescu, Integrated architectures of electrodes and flexible porous substrates for point-of-care testing, *Curr. Opin. Electrochem.*, 2023, **42**, 101418.
  - 34 X. Liao, H. Fu, T. Yan and J. Lei, Electroactive metal-organic framework composites: design and biosensing applications, *Biosens. Bioelectron.*, 2019, **146**, 111743.
  - 35 B. Zhang, J. Zhang, X. Tan, D. Shao, J. Shi, L. Zheng, J. Zhang, G. Yang and B. Han, MIL-125-NH<sub>2</sub>@TiO<sub>2</sub> Core-Shell Particles Produced by a Post-Solvothermal Route for High-Performance Photocatalytic H<sub>2</sub> Production, *ACS Appl. Mater. Interfaces*, 2018, **10**, 16418–16423.
  - 36 R. T. Massah, T. J. M. M. Ntep, E. Njanja, S. L. Z. Jiokeng, J. Liang, C. Janiak and I. K. Tonle, A metal-organic framework-based amperometric sensor for the sensitive determination of sulfite ions in the presence of ascorbic acid, *Microchem. J.*, 2021, **169**, 106569.
  - 37 S. Zhao, Y. Wang, J. Dong, C. T. He, H. Yin, P. An, K. Zhao, X. Zhang, C. Gao, L. Zhang, J. Lv, J. Wang, J. Zhang, A. M. Khattak, N. A. Khan, Z. Wei, J. Zhang, S. Liu, H. Zhao and Z. Tang, Ultrathin Metal-Organic Framework Nanosheets for Electrocatalytic Oxygen Evolution, *Nat. Energy*, 2016, **1**, 16184.
  - 38 Q. Yang, Q. Xu and H. L. Jiang, Metal-Organic Frameworks Meet Metal Nanoparticles: Synergistic Effect for Enhanced Catalysis, *Chem. Soc. Rev.*, 2017, **46**, 4774–4808.
  - 39 K. E. DeKrafft, C. Wang and W. B. Lin, Metal-Organic Framework Templated Synthesis of Fe<sub>2</sub>O<sub>3</sub>/TiO<sub>2</sub> Nanocomposite for Hydrogen Production, *Adv. Mater.*, 2012, **24**, 2014–2018.
  - 40 R. V. Jagadeesh, K. Murugesan, A. S. Alshammari, H. Neumann, M. M. Pohl, J. Radnik and M. Beller, MOF-Derived Cobalt Nanoparticles Catalyze A General Synthesis of Amines, *Science*, 2017, **358**, 326–332.
  - 41 Y. Zhang<sup>1</sup>, J. Song, Q. Pan, X. Zhang, W. Shao, X. Zhang and C. J. Quan, and Li, An Au@NH<sub>2</sub>-MIL-125(Ti)-based multifunctional platform for colorimetric detections of biomolecules and Hg<sup>2+</sup>, *J. Mater. Chem. B*, 2020, **8**, 114.
  - 42 Y. Bao, J. Song, Y. Mao, D. Han, F. Yang, L. Niu and A. Ivaska, Graphene Oxide-Templated Polyaniline Microsheets toward Simultaneous Electrochemical Determination of AA/DA/UA, *Electroanalysis*, 2011, **23**, 878–884.
  - 43 M. Sohail, Y.-N. Yun, E. Lee, S. K. Kim, K. Cho, J.-N. Kim, T. W. Kim, J.-H. Moon and H. Kim, MIL-125(Ti) with S-Shaped water Isotherms for adsorption Heat Transformation, *Cryst. Growth Des.*, 2017, **17**, 1208–1213.
  - 44 M. Z. Hussain, M. Bahri, W. R. Heinz, Q. Jia, O. Ersen, T. Kratky, R. A. Fischer, Y. Zhu and Y. Xia, An in situ investigation of the thermal decomposition of metal-organic framework NH<sub>2</sub>-MIL-125(Ti), *Microporous Mesoporous Mater.*, 2021, **316**, 110957.
  - 45 X. Zhang, Z. Chen, Y. Luo, X. Han, Q. Jiang, T. Zhou, H. Yang and J. Hu, Construction of NH<sub>2</sub>-MIL-125(Ti)/CdS Z-scheme heterojunction for efficient photocatalytic H<sub>2</sub> evolution, *J. Hazard. Mater.*, 2021, **405**, 124128.
  - 46 H. Zhao, Z. Xing, S. Su, S. Song, Z. Li and W. Zhou, Gear-shaped mesoporous NH<sub>2</sub>-MIL-53(Al)/CdS P-N heterojunctions as efficient visible-light-driven photocatalysts, *Appl. Catal., B*, 2021, **291**, 120106.
  - 47 J. Stejskal and R. G. Gilbert, Polyaniline. preparation of a conducting polymer, *Pure Appl. Chem.*, 2002, **74**, 857–867.
  - 48 M. Karabacak, M. Cinar, Z. Unal and M. Kurt, FT-IR, UV spectroscopic and DFT quantum chemical study on the molecular conformation, vibrational and electronic transitions of 2-aminoterephthalic acid, *J. Mol. Struct.*, 2010, **982**, 22–27.
  - 49 M. Oveisi, M. A. Asli and N. M. Mahmoodi, MIL-Ti metal-organic frameworks (MOFs) nanomaterials as superior



- adsorbents: Synthesis and ultrasound-aided dye adsorption from multicomponent wastewater systems, *J. Hazard. Mater.*, 2018, **347**, 123–140.
- 50 T. K. Patil and M. I. Talele, Comparative study of semiconductors bismuth iodate, bismuth triiodide and bismuth trisulphide crystals, *Adv. Appl. Sci. Res.*, 2012, **3**, 1702–1708.
  - 51 R. Zamiri, H. A. Ahangar, A. Zakaria, G. Zamiri, M. Shabani, B. Singh and J. M. F. Ferreira, The structural and optical constants of Ag<sub>2</sub>S semiconductor nanostructure in the Far-Infrared, *Chem. Cent. J.*, 2015, **9**, 1–6.
  - 52 J. Qiu, L. Yang, M. Li and J. Yao, Metal nanoparticles decorated MIL-125-NH<sub>2</sub> and MIL-125 for efficient photocatalysis, *Mater. Res. Bull.*, 2019, **112**, 297–306.
  - 53 K. L. T. Nguena, C. G. Fotsop, S. B. L. Ngomade, A. K. Tamo, C. A. Madu, F. I. Ezema and E. E. Oguzie, Mathematical modeling approach for the green synthesis of high-performance nanoporous zeolites Na-X optimized for water vapor sorption, *Mater. Today Commun.*, 2023, **37**, 107406.
  - 54 S. B. L. Ngomade, C. G. Fotsop, K. L. T. Nguena, I. K. Tchummegne, M. L. T. Ngueteu, A. K. Tamo, G. Ndifor-Angwafor Nche and S. G. Anagho, Catalytic performances of CeO<sub>2</sub>@SBA-15 as nanostructured material for biodiesel production from Podocarpus falcatus oil, *Chem. Eng. Res. Des.*, 2023, **194**, 789–800.
  - 55 A. V. Somba, E. Njanja, G. Deffo, C. G. Fotsop, K. Y. Tajou, A. F. T. Njiemou, F. Eya'ane Meva and T. Kamgaing, Evaluation of Silver Nanoparticles Based on Fresh Cocoa Pods (*Theobroma Cacao*) Extracts as New Potential Electrode Material, *J. Chem.*, 2023, **14**, 6447994.
  - 56 S. Kim, J. Kim, H. Kim, Y. H. Cho and W. S. Ahn, Adsorption/catalytic properties of MIL-125 and NH<sub>2</sub>-MIL-125, *Catal. Today*, 2013, **204**, 85–93.
  - 57 G. Deffo, R. C. T. Temgoua, S. F. Mbokou, E. Njanja, I. K. Tonlé and E. Ngameni, A sensitive voltammetric analysis and detection of Alizarin Red S onto a glassy carbon electrode modified by an organosmectite, *Sens. Int.*, 2021, **2**, 100126.
  - 58 G. Deffo, R. C. T. Temgoua, K. Y. Tajou, E. Njanja, G. Doungmo, I. K. Tonle and E. Ngameni, Signal amplification by electropolymerization of alizarin red S for improved diuron detection at organosmectite modified glassy carbon electrode, *J. Chin. Chem. Soc.*, 2021, 1–10.
  - 59 C. Zhang, Z. Xiao, T. Qin and Z. Yang, Mechanism and kinetics of uric acid adsorption on nanosized hydroxyapatite coating, *J. Saudi Chem. Soc.*, 2019, **23**, 249–253.
  - 60 S. G. Fogang, G. Deffo, L. S. Guenang, R. C. T. Temgoua, E. Njanja, I. K. Tonlé, A. Bhaumik and E. Ngameni, Nafion/Multiwalled Carbon Nanotubes/Mesoporous Silica Composite Modified Glassy Carbon Electrode for the Simultaneous Electrochemical Determination of Indigo Carmine and Carbazepine by Differential Pulse Voltammetry, *Anal. Lett.*, 2023, 1–17.
  - 61 L. Yang, D. Liu, J. Huang and T. You, Simultaneous determination of dopamine, ascorbic acid and uric acid at electrochemically reduced graphene oxide modified electrode, *Sens. Actuators, B*, 2014, **193**, 166–172.
  - 62 C. Wang, J. Du, H. Wang, C. Zou, F. Jiang, P. Yang and Y. Du, A facile electrochemical sensor based on reduced graphene oxide and Au nanoplates modified glassy carbon electrode for simultaneous detection of ascorbic acid, dopamine and uric acid, *Sens. Actuators, B*, 2014, **204**, 302–309.
  - 63 D. Han, T. Han, C. Shan, A. Ivaska and L. Niua, Simultaneous Determination of Ascorbic Acid, Dopamine and Uric Acid with Chitosan-Graphene Modified Electrode, *Electroanalysis*, 2010, **22**, 2001–2008.
  - 64 L. Fu, A. Wang, G. Lai, W. Su, F. Malherbe, J. Yu, C.-T. Lin and A. Yu, Defects regulating of graphene ink for electrochemical determination of ascorbic acid, dopamine and uric acid, *Talanta*, 2018, **180**, 248–253.
  - 65 X. Ouyang, L. Luo, Y. Ding, B. Liu, D. Xu and A. Huang, Simultaneous determination of uric acid, dopamine and ascorbic acid based on poly(bromocresol green) modified glassy carbon electrode, *J. Electroanal. Chem.*, 2015, **748**, 1–7.
  - 66 Q. Zhu, J. Bao, D. Huo, M. Yang, H. Wu, C. Hou, Y. Zhao, X. Luo and H. Fa, 3DGH-Fc based electrochemical sensor for the simultaneous determination of ascorbic acid, dopamine and uric acid, *J. Electroanal. Chem.*, 2017, **799**, 459–467.
  - 67 Y. Bao, J. Song, Y. Mao, D. Han, F. Yang, L. Niu and A. Ivaska, Graphene Oxide-Templated Polyaniline Microsheets toward Simultaneous Electrochemical Determination of AA/DA/UA, *Electroanalysis*, 2011, **23**, 878–884.
  - 68 T. S. Thanh, P. T. Qui, N. T. T. Tu, T. T. T. Toan, T. T. B. Hoa, L. V. T. Son, D. M. Nguyen, T. N. Tuyen and D. Q. Khieu, Electrochemical Determination of Uric Acid in Urine by Using Zeolite Imidazolate Framework-11 Modified Electrode, *J. Nanomater.*, 2021, **2021**, 1–13.
  - 69 Z. Hadi and K. h Ghanbari, A novel electrochemical sensor for determination of uric acid in the presence of ascorbic acid and dopamine based on a carbon paste electrode modified with an electrochemically reduced *para*-nitrobenzoic acid/graphene oxide nanocomposite, *New J. Chem.*, 2022, **46**, 12941–12951.

